Plant Soil (2020) 454:261–281
https://doi.org/10.1007/s11104-020-04653-7

METHODS PAPER

Imaging plant responses to water deficit using electrical resistivity tomography

Sathyanarayan Rao · Nolwenn Lesparre · Adrián Flores-Orozco · Florian Wagner · Andreas Kemna · Mathieu Javaux

Received: 17 April 2020 / Accepted: 26 July 2020 / Published online: 1 August 2020
© The Author(s) 2020, corrected publication 2020

Abstract

Background and aims Monitoring root water uptake dynamics under water deficit (WD) conditions in fields are crucial to assess plant drought tolerance. In this study, we investigate the ability of Electrical Resistivity Tomography (ERT) to capture specific soil water depletion induced by root water uptake.

Methods A combination of surface and depth electrodes with a high spatial resolution (10 cm) was used to map 2-D changes of bulk soil electrical conductivity (EC) in an agronomic trial with different herbaceous species. A synthetic experiment was performed with a mechanistic model to assess the ability of the electrode configuration to discriminate abstraction patterns due to roots. The impact of root segments was incorporated in the forward electrical model using the power-law mixing model.

Results The time-lapse analysis of the synthetic ERT experiment shows that different root water uptake patterns can be delineated for measurements collected under WD conditions but not under wet conditions. Three indices were found (depletion amount, maximum depth, and spread), which allow capturing plant-specific water signatures based moisture profile changes derived from EC profiles. When root electrical properties were incorporated in the synthetic experiments, it led to the wrong estimation of the amount of water depletion, but a correct ranking of plants depletion depth. When applied to the filed data, our indices showed that Cocksfoot and Ryegrass had shallower soil water depletion zones than white clover and white clover combined with Ryegrass. However, in terms of water depletion amount, Cocksfoot consumed the largest amount of water, followed by White Clover, Ryegrass+White Clover mixture, and Ryegrass.

Conclusion ERT is a well-suited method for phenotyping root water uptake ability in field trials under WD conditions.

Keywords Electrical resistivity tomography. Soil-root modeling. Hydrogeophysics. Crop imaging. Geophysical inversion

Responsible Editor: Peter J. Gregory.

Electronic supplementary material The online version of this article (https://doi.org/10.1007/s11104-020-04653-7) contains supplementary material, which is available to authorized users.

S. Rao (✉) · M. Javaux
Department of Environmental Sciences, Earth and Life Institute, Université Catholique de Louvain, Louvain-la-Neuve, Belgium
e-mail: Sathyanarayan.rao@uclouvain.be

N. Lesparre
Laboratoire d'Hydrologie et Géochimie de Strasbourg, University of Strasbourg/EOST/ENGEES, CNRS UMR 7517, 1 Rue Blessig, 67084 Strasbourg, France

A. Flores-Orozco
Geophysics Research Group, Vienna University of Technology, Gusshausstraße 27-29, E120-3, 1040 Vienna, Austria

F. Wagner
Institute for Applied Geophysics and Geothermal Energy, RWTH Aachen University, Aachen, Germany

A. Kemna
Geophysics Section, Institute of Geosciences, University of Bonn, Bonn, Germany

M. Javaux
Agrosphere, IBG3, Forschungszentrum Jülich GmbH, Jülich, Germany

Abbreviations

ERT	Electrical Resistivity Tomography
WD	Water deficit
TDR	Time Domain Reflectometry
C	Cocksfoot (C)
R + WC	Ryegrass+White clover mixture
WC	White clover (WC)
R	Ryegrass
RND	Root number density
VGM	Van-Genuchten Mualem
ET0	Evapotranspiration
rrms	Root mean square error

Introduction

Developing and characterizing crops tolerant to drought and able to keep high yields under limited soil water resources are key challenges to face increasing global food demand in a changing environment. Root systems control plant access to soil water and are thus key organs for drought tolerance. Plant breeders are interested to optimize plant performances by understanding the soil exploration dynamics of roots, their reaction to the spatial distribution of soil water, and root hydraulic properties between root orders and age (Meunier et al. 2020). Yet, the ability to accurately, and extensively characterize root traits or phenes (i.e. characteristic features) is a major challenge in the field of root biology (Meister et al. 2014). Novel root phenotyping techniques, i.e., tools to characterize root system properties and functions in situ (Atkinson et al. 2019) are instrumental to develop these new genotypes. Typically, most of the current root phenotyping is performed on young plants grown in aeroponics, or small containers filled with non-natural substrates. Plant's ability to deal with the heterogeneous environment is therefore difficult to assess. Recognizing the limiting interest of root phenotyping in pots, Passioura (2012) suggested that field phenotyping is needed to ensure that plant genotypes can deal with the natural temporal and spatial variability of the environment.

Root water uptake distribution is a key factor to assess plant tolerance and adaptation to water deficit (WD) conditions. Root water uptake is not the only function of root system architecture and soil water availability, but also of root hydraulics (Leitner et al. 2014; Meunier et al. 2017). Hence, the dynamics of root water uptake reveals plant functioning, in particular under WD. Yet, root water fluxes are impossible to monitor in the field, and often soil water depletion resulting from root uptake is measured instead. However, soil water depletion patterns cannot always be linked to root water uptake distribution due to soil water movements (Vandoorne et al. 2012). In wet conductive soils, water uptake can take place without a change of soil moisture, for instance. To associate water depletion to uptake patterns, soil water fluxes must be limited.

Recently Cimpoiaşu et al. (2020) reviewed specific advantages and limitations of geoelectrical methods to monitor root zone processes and structure and showed that Electrical Resistivity Tomography (ERT) is well suited to monitor soil water content evolution and thus soil water depletion patterns in situ. High-resolution root-zone soil moisture monitoring can reveal the differences between the root system of different species under varying climatic conditions. For example, monitoring soil water depletion patterns via ERT has shown to provide useful information on root density (Amato et al. 2008; Paglis 2013), soil compaction due to tillage (Besson et al. 2004), soil water content (Michot et al. 2003; Garré et al. 2011; Beff et al. 2013; Dahlin et al. 2014) thereby promising itself as a valuable tool to monitor soil-root system.

Most studies usually analyzed absolute resistivity obtained from surface ERT. For example, Panissod et al. (2008) demonstrated that 2D ERT obtained resistivity information could be used to investigate soil water patterns in maize fields. Brillante et al. (2015) applied ERT to identify water movements and active uptake zones in a vineyard. Ain-Lhout et al. (2016) monitored soil moisture in the root zone system of a tree. Mares et al. (2016) studied the evolution of soil and tree water content using 2-D ERT. Monitoring temporal change of resistivity using ERT instead of absolute resistivity has some advantages in eliminating artifacts due to bad contact electrodes and is being used in the number of soil-root studies. Boaga et al. (2013) used time-lapse ERT to study water uptake dynamics in the apple orchard farm. Jayawickreme et al. (2008) used temporal changes in resistivity to compare forest with grasslands. Garré et al. (2013) showed that in an inter-cropped field, the ERT method could distinguish the depth of soil water depletion for different plant species and also differentiate fertilized and unfertilized treatments when analyzed in temporal changes of water content instead of absolute resistivity. Srayeddin and Doussan (2009)

used ERT to compare soil water depletion patterns of maize and Sorghum and found Sorghum to be more efficient in water extraction as compared to Maize. In their studies only when the temporal difference in resistivity or water content were analyzed the comparison between species became apparent. However, in water stress treatment, the water uptake front could not be quantified beyond 50–60 cm depth due to poor sensitivity of surface electrode configuration (Srayeddin and Doussan 2009). Recently, Benjamin et al. (2020) used time-lapse electrical resistivity tomography and mise-à-la-masse to monitor root distributions in a vineyard. More recently, Whalley et al. (2017) successfully used surface ERT at field scale to distinguish wheat genotypes based on their soil water profile evolution. They concluded that ERT was a promising tool for phenotyping because of its ability to characterize deep changes of electrical resistivity, and its higher sensitivity to dry soil.

However, ERT faces several challenges when used for field phenotyping. Small differences in rooting or water uptake depths between genotypes might result in large differences in terms of drought tolerance (Manschadi et al. 2006), which means that high spatial resolution is needed. Therefore, the contrast between uptake patterns of different genotypes is not always visible with ERT (Whalley et al. 2017). Also, the sensitivity of ERT measurements to root and soil water depletion is not always sufficient (Rao et al. 2019), and can even be decreased by additional processes such as solute distribution or too wet soil conditions. Furthermore, commonly used surface electrode configuration may not be suitable for phenotyping roots that need higher spatial resolution in the sub-meter scale where differences between different root systems occur (Srayeddin and Doussan 2009). Because of the ill-posed nature of ERT inversion, it is necessary to differentiate the changes observed in ERT inversions in terms of artifacts and physiology of plants to have meaningful results.

In this study, our general objective is to investigate the ability of ERT to detect slight differences in depletion depths between plant species in a quantitative way. Our specific questions were (i) how to analyze ERT field data to detect slight changes in water depletion? (ii) what is the spatial resolution that is needed and that can be achieved to discriminate plant uptake behaviors? To answer these questions, we develop a new quantitative approach to discriminate soil water abstraction amount, depth, and spread based on a synthetic experiment with a process-based model in which we included the uncertainty in petrophysical relation (Rao et al. 2019). This methodology was then used to interpret 2-D ERT field data in an agronomic field trial comparing different herbaceous species, with potentially different root systems functioning as a test for our method.

Materials and methods

Field trial description

The experimental field is located in Corroy-le-Grand (Belgium), in the De Marbais University farm. A random-block field trial was established in 2012 for comparing combinations of three herbaceous species under two contrasted treatments: control (normal weather conditions) and WD through a shelter preventing rainfall for six weeks. The whole field trial was organized in blocks (7.2 m × 7 m) made of four plots (1.5 m width × 7 m length each) with a separation of 30 cm between plots (Fig. 1). In this study, we focused on four plots with the following species: cocksfoot (C), ryegrass+white clover mixture (R + WC), white clover (WC) and ryegrass (R). Cocksfoot (*Dactylis glomerata*) and ryegrass (*Lolium perenne*) are both deep-rooted perennial grasses. White clover (*Trifolium repense)* is a perennial legume plant commonly grown in mixture with ryegrass in pastures. It is typically described as a shallow-rooted plant but its root system can reach 1 m-depth (Nichols et al. 2016).

The soil type is a luvisol (loamy soil developed on loess) with 6 different soil horizons: Ap1, Ap2, Ap3, Bt1, Bt2, and C in WD treatment and 5 soil horizons in control (all except Bt2) as shown in Fig. 1b. Due to natural heterogeneity, the WD and control treatment zones had slightly different soil horizons as revealed by soil trenches (Fig. 1b). Soil trenches were dug to estimate root distribution profiles for each species in each plot using the Tardieu profile method (Tardieu 1988). We used a grid of 5 cm × 5 cm to count the root numbers to obtain a 2-D distribution of Root Number Density (*RND*) at the end of the season.

The soil hydraulic properties were characterized using the evaporation method (Bezerra-Coelho et al. 2018) on 250 cm^3 undisturbed soil cores sampled from the different horizon and the Hyprop-fit software (Pertassek et al. 2015) to fit the experimental data with the Van-Genuchten-Mualem (VGM) soil hydraulic model. A nearby weather station provided the potential evapotranspiration (ET0) and precipitation data. The

potential evapotranspiration, precipitation, and root number density distributions are shown in Fig. 2.

Field ERT

ERT data acquisition

In 2016, surface and depth ERT electrodes were installed regularly along 2-D planes, each of them crossing the middle of four plots (see Fig. 1a): one in WD, the other one in control conditions.

For ERT data acquisition, we used 123 electrodes, including 48 placed on the surface (with a separation of 0.15 m) and 75 electrodes distributed along 13 boreholes (Fig. 3). Boreholes were made of PVC sticks, with embedded stainless-steel rings used as electrodes, with a diameter of 46 mm for each ring (same as Beff et al. 2013), the separation between electrodes increases with depth (Fig. 1a). Between each pair of boreholes, we placed four surface electrodes.

The ERT data was collected using an ARES II 10-channel automatic resistivity system (from GF instruments®). ERT monitoring data set consisted of three-time stamps (denoted by t1 to t3), with data collected along the experimental block every week along three consecutive weeks. The exact dates of measurements were t1: 03/08/2017, t2: 09/08/2017, and t3:16/08/2017. For the ERT measurements, we used current injections with 100% duty cycle, with a pulse length of 300 ms, and stacking varying between 3 and 4 repetitions.

The injection scheme comprised of 3084 quadrupoles, out of which 450 quadrupoles were reciprocal readings (collection of the same quadrupole after interchanging the current and potential dipoles). To describe the configuration in the injection scheme, we denote current injecting electrodes as AB and potential measuring electrodes as MN. The injection scheme used in the experiment is categorized into:

a) Scheme 1 (Surface measurements only): Gradient (Schlumberger) and dipole-dipole configuration (Dahlin and Zhou 2006) among the 48 surface electrodes spanning 7.2 m representing 20% of total quadrupoles. The dipole-dipole scheme consisted of skip-0 (dipole spacing of one electrode or 15 cm), skip-1 (dipole spacing of two electrodes or 30 cm), and skip-2 (dipole spacing of three electrodes or 45 cm) protocols. Each current injection consisted of five potential measurements with a separation varying from 15 to 45 cm. Gradient configuration had a maximum current electrode separation distance of 60 cm and each current injection had 5 simultaneous potential measurements with a dipole spacing of 1 to 3 electrodes (15 to 45 cm).
b) Scheme 2 (Boreholes only): (i) AB on a given borehole and MN on its adjacent borehole, and (ii) AM on a given borehole and BN on its adjacent borehole. Only two adjacent boreholes were used in the injection scheme, i.e., there was no measurement or injection between the first and third borehole. This scheme represented about 20% of the total quadrupoles.
c) Scheme 3 (Surface-borehole interacting scheme): AB (or MN) on surface electrodes located between any two borehole sticks and MN (or AB) on boreholes situated directly below surface electrodes with a dipole spacing of one or two for current injection and for each AB we had five to seven MN's with skip-0 and skip-1 spacing. This scheme represented the remaining 60% of the total quadrupoles.

ERT inversion theory

We used the pyGIMLi software (Rücker et al. 2017) for the inversion of the ERT data sets. In the inversion algorithm, the Gauss-Newton scheme is used to iteratively minimize the objective function (ϕ):

$$\phi = \phi_d + \lambda\phi_m = \left\| \frac{\overline{d} - f(\overline{m})}{\log(1 + E_{model})} \right\|_2^2 + \lambda \| W(\overline{m} - \overline{m}_0) \|_2^2 \quad (1)$$

where ϕ_d corresponds to the data misfit between the measured data vector ($\overline{d}$) and the data estimated by the model ($f(\overline{m})$) down-weighted by the error model (E_{model}). ϕ_m represents the model misfit and is multiplied by the regularization parameter λ determining the weighting of the model versus data misfits. $\overline{d}$ stands for the log of measured apparent resistivities from real/numerical experiments, $\overline{m}_0$ is a homogeneous starting model vector, W is a first-order smoothness regularization matrix used to stabilize the inverse problem that is inherently ill-posed. An L2-norm is adopted as smoothed shapes of the subsurface properties are inferred. The regularization is made anisotropic by having a smaller value for smoothness in the vertical direction

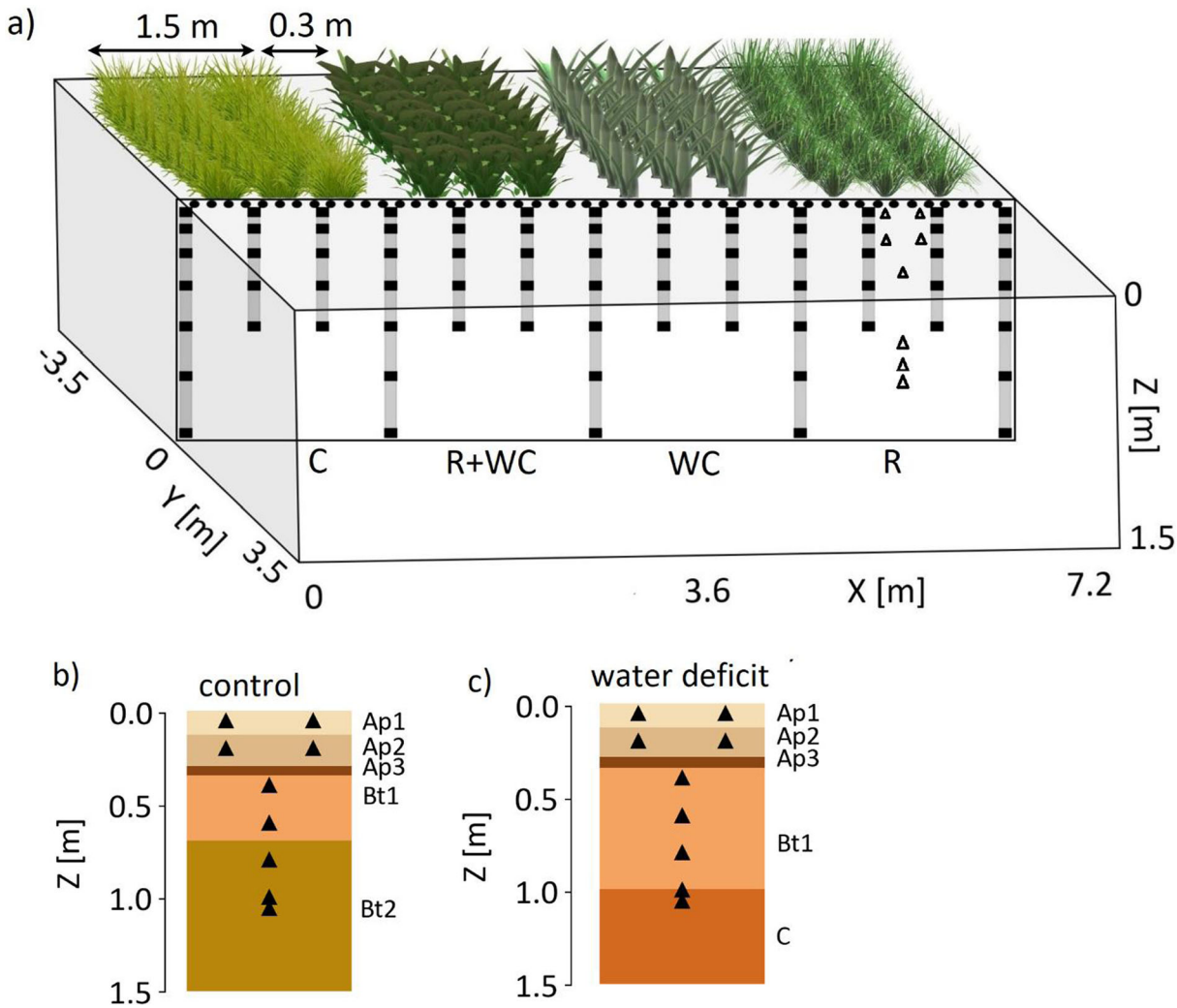

Fig. 1 **a**) A schematic view of an individual block showing the ERT electrodes at the center plane (y = 0) used for two-dimensional ERT imaging. The black dots represent the surface point electrodes while the black squares are the borehole ring electrodes. Inside the ERT block, one binary mixture (R + WC: ryegrass+white clover) and three monocultures (C: cocksfoot; WC: white clover; R: ryegrass) are present. Location of TDR probes (triangles) installed at different depths in the ryegrass plot. Different soil-horizons are indicated along with TDR locations (triangles) for b) control and c) water deficit treatments

as compared to the horizontal direction for resolving horizontal layering of soil horizons.

We quantified field data error using the analysis of normal-reciprocal misfit, first described by LaBrecque et al. (LaBrecque et al. 1996). In our measurements, we computed an absolute error of 0.04 Ω and a relative error of 12% (see supplement S2 for details). The optimum regularization constant λ was determined using L-curve analysis (Hansen 1992; Bergmann et al. 2017). For different values of λ ranging from 5 to 1000, we computed ϕ_d and ϕ_m. The λ value for which the ϕ_d vs ϕ_m curve has a minimum distance to the origin is chosen as the optimum value (see supplement S3 for details).

The ratio by which λ is reduced for vertical contrast is determined by Z_w that is fixed to 0.5 meaning that the smoothness regularization strength in the vertical direction is half of the horizontal one. We chose Z_w of 0.5 and a λ of 150 for the inversion of synthetic data. We found that the choice of Z_w played an important role in reducing inversion artifacts and the chosen value of 0.5 produced least artifacts when visually as well as quantitatively compared with the original model (see supplement S4 for details).

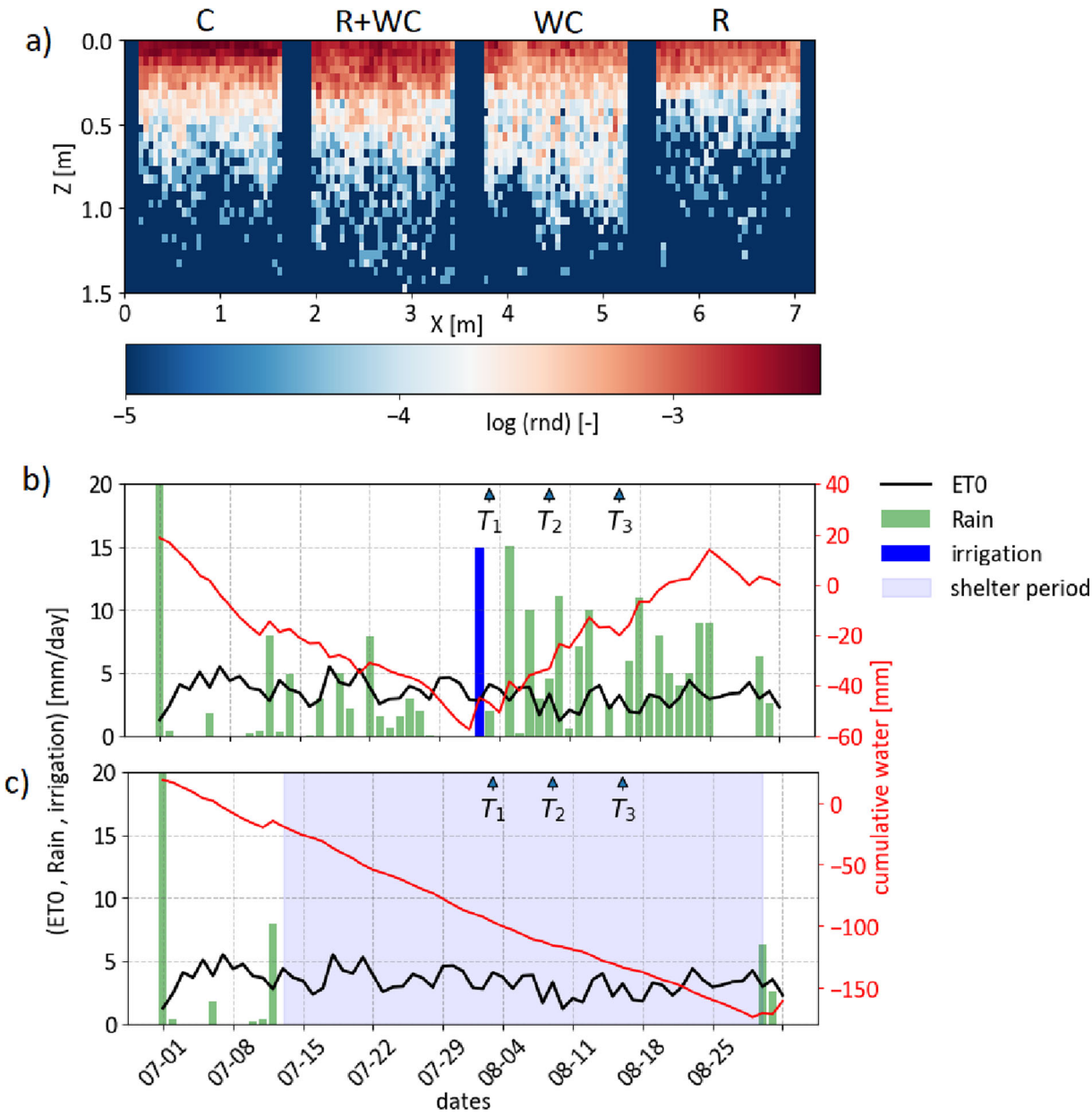

Fig. 2 **a**) Log of root number density measured in the field, **b**) weather condition in the control plot and **c**) weather condition in water deficit plot

We used the relative root mean square error (rrms) and chi-square χ^2 value to assess the quality of inversion:

$$rrms = \sqrt{\frac{\sum\left[\frac{\overline{d}-f(\overline{m})}{\overline{d}}\right]^2}{N}}.100\% \quad (2)$$

$$\chi^2 = \frac{\sum\left[\frac{\overline{d}-f(\overline{m})}{Emodel}\right]^2}{N} \quad (3)$$

where N is the length of the data vector ($\overline{d}$). Here the inversion is stopped when the rrms value reaches 2% or χ^2 is around 5 to 8 (Günther and Rücker 2006). Optimized resistivity fields were then temperature-corrected at 25 °C (Luo et al. 2019) based on field thermometers (see next section) assuming homogeneous lateral temperature distribution and linear depth interpolation.

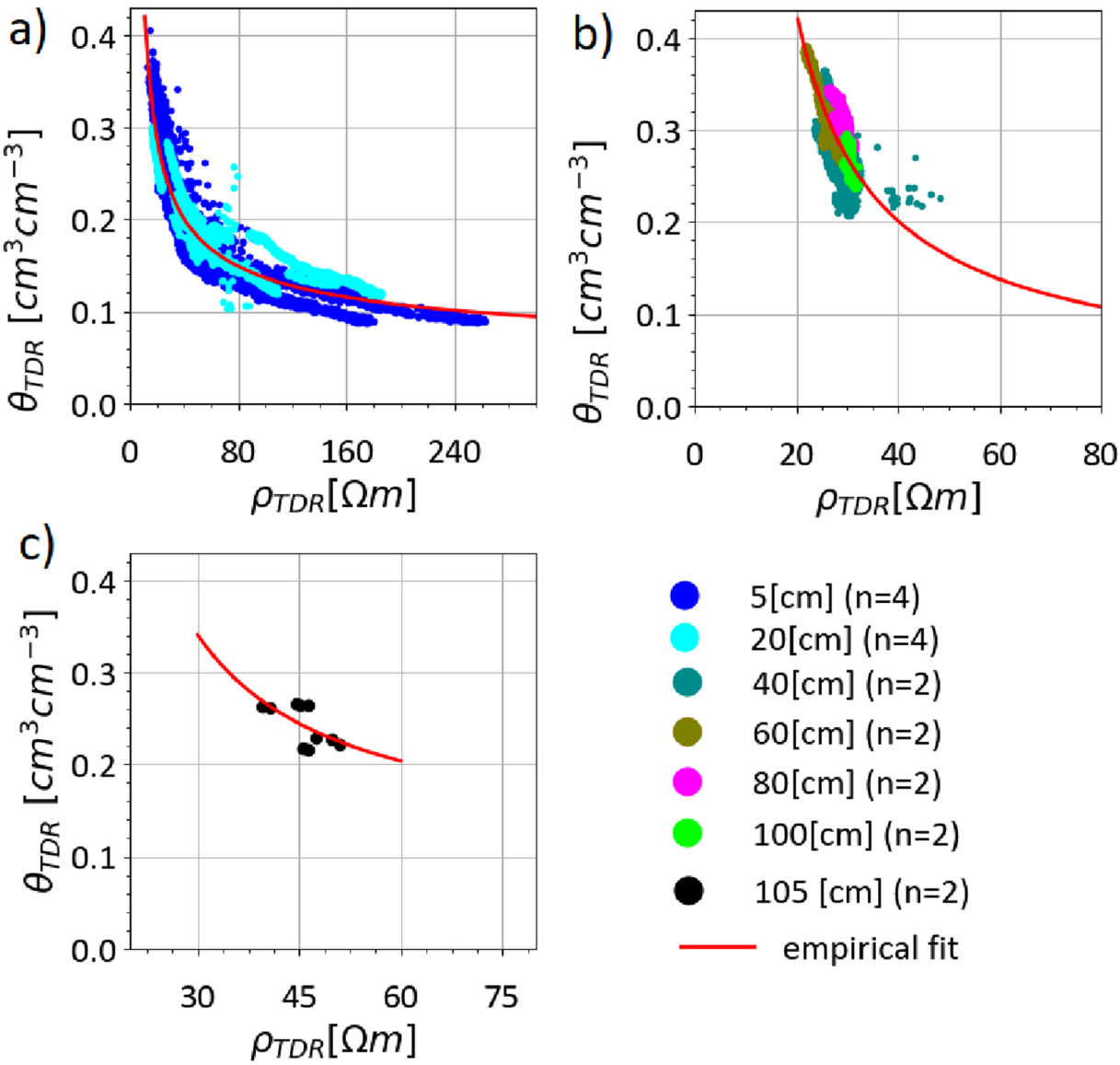

Fig. 3 Combined TDR measurements in 2018 for water deficit and control conditions (electrical conductivity (σ_{TDR}) versus water content θ)) at different soil horizons: a) Ap layer, **b**) Bt layer, and **c**) C layer. The color in the scatter plot indicates the depth of the TDR probes and n is the no. of probes. The red line represents the empirical model fit [Eq.4] to the data

Time domain Reflectometry (TDR) and Petrophysical model

Besides ERT, we installed nine TDR probes along with the ryegrass plant plot at different depths (i.e., soil horizons) for monitoring on an hourly basis soil water content (θ_{TDR}) and electrical resistivity (ρ_{TDR}) from 29/05/2018 to 26/10/2018. Temperature sensors were installed at the same depths as the TDR for electrical resistivity temperature correction. We followed a 2% decrease in electrical resistivity per degree centigrade (Beff et al. 2013; Whalley et al. 2017; Luo et al. 2019).

A median filter with a window size of 3 h was used to filter out the outliers in ρ_{TDR} and θ_{TDR}. The filtered data were combined per groups of the pedological horizon (Ap and Bt) for WD and control conditions and used to characterize soil petrophysical functions per horizon, by fitting the following model:

$$\theta = a\ log_{10}(\rho)^b + \theta r \quad (4)$$

where a and b are the fitting parameters, θr is the residual water content. The fitting parameters for each soil horizons along with RMSE of fits are given in Table 1, and θr is 0 except for the C layer (Table 2). The fits along with the TDR data are shown in Fig. 3.

Numerical experiments

We conducted a synthetic experiment with the following objectives: (1) to evaluate the reliability of the ERT injection scheme to capture the variability of subsurface resistivity in terms of coverage; (2) to investigate the ability of ERT to discriminate different root water uptake pattern evolutions; (3) to formulate ERT-derived indices, able to quantify the uptake behavior of plants and (4) to investigate how petrophysical relation including root electrical properties might impact our results. Figure 4 describes the detailed workflow for the numerical experiment and its connection to real field data interpretation. We combined water-flow simulations (blue in Fig. 4) with forward and inverse ERT simulations (red in Fig. 4) to generate synthetic experiments representing potential ERT field observations to later compare with real field data.

Water flow simulations

We used the mechanistic soil-plant water flow model R-SWMS (Javaux et al. 2008, 2013) to simulate the evolution of soil water content distributions in the field trial for 3 weeks (between 03/08/2017 and 16/08/2017). R-SWMS is a validated process-based model (Koch et al. 2019), which predicts plant actual transpiration and 3-D root and soil water uptake fluxes based on soil and plant hydraulic properties and a potential evapotranspiration demand (ET0). The simulation domain is a block of 7.2 m × 0.1 m × 1.5 m crossing the middle of the 4 plots corresponding to the location of the vertical ERT electrode plane. Two simulations were run: one for the control and one for the WD conditions, with the corresponding, observed rainfall, irrigation and evapotranspiration times series.

Table 1 Empirical fitting parameters found using non-linear optimization presented in Eq. [4] for different soil horizon and their corresponding RMSE.

Horizon	a	b	θr	*RMSE*
Ap (Ap1, Ap2, Ap3)	0.4528	−1.7299	0	0.017
Bt (Bt1, Bt2)	1.107	−3.619	0	0.025
C	18.8792	−9.0224	0.1	0.012

Table 2 Relative percentage error of Gaussian fit parameters between R-SWMS simulated change of water content ($\delta\theta_{fwd}$) and ERT inverted change of water content ($\delta\theta_{inv}$) for different scenarios

Scenario	Gaussian fit parameters	$\left\lvert\frac{\delta\theta_{fwd}-\delta\theta_{inv}}{\delta\theta_{fwd}}\right\rvert$ %			
1	$A_{\delta\theta}$	**C**	**R + WC**	**WC**	**R**
		3.18314	33.8091	7.79448	17.653
	$\mu_{z,\delta\theta}$	0.021121	6.41863	3.32526	4.00994
	$\sigma_{z,\delta\theta}$	19.408	13.2332	12.6652	43.2708
2	$A_{\delta\theta}$	17.1256	20.1984	4.55819	15.5163
	$\mu_{z,\delta\theta}$	3.96602	6.29113	4.44595	4.05132
	$\sigma_{z,\delta\theta}$	20.3411	12.8036	5.41698	42.8032
3	$A_{\delta\theta}$	42.3186	39.3282	40.0956	19.3176
	$\mu_{z,\delta\theta}$	2.33008	12.7311	7.78745	5.07675
	$\sigma_{z,\delta\theta}$	2.33873	28.8829	6.44379	33.5639

The soil domain consisted of five layers corresponding to the observed soil horizons shown in Fig. 1b and c (control and WD treatments have a slightly different horizon distribution). Soil hydraulic properties of each layer are parameterized with the VGM model (see Table S1 in the supplement S5).

The soil boundary conditions for the control treatment consisted of the precipitation time series from weather station complemented by manual irrigation (Fig. 2c). Free drainage was used as a soil bottom boundary condition. For WD treatment, a no-flux soil top boundary condition was used as neither rainfall nor irrigation happened during the simulation period. Evaporation fluxes between plots were neglected. To generate realistic 3-D initial conditions at the beginning of our experimental period, we ran the warm-up for 30 days. The initial soil condition at time − 30 days was hydrostatic equilibrium with a saturated soil at the depth of −316 cm.

Root water uptake of the different plant species was simulated using the macroscopic parameterization proposed by Couvreur et al. (2012). We normalized the measured *RND* of the 4 plots as a proxy for soil uptake fraction (*SUF*) distribution (Fig. 2b). We assumed that the equivalent conductance of the root system (*Krs*) equals the compensatory root water uptake conductance (*Kcomp*) (see Table S2 of supplementary material).

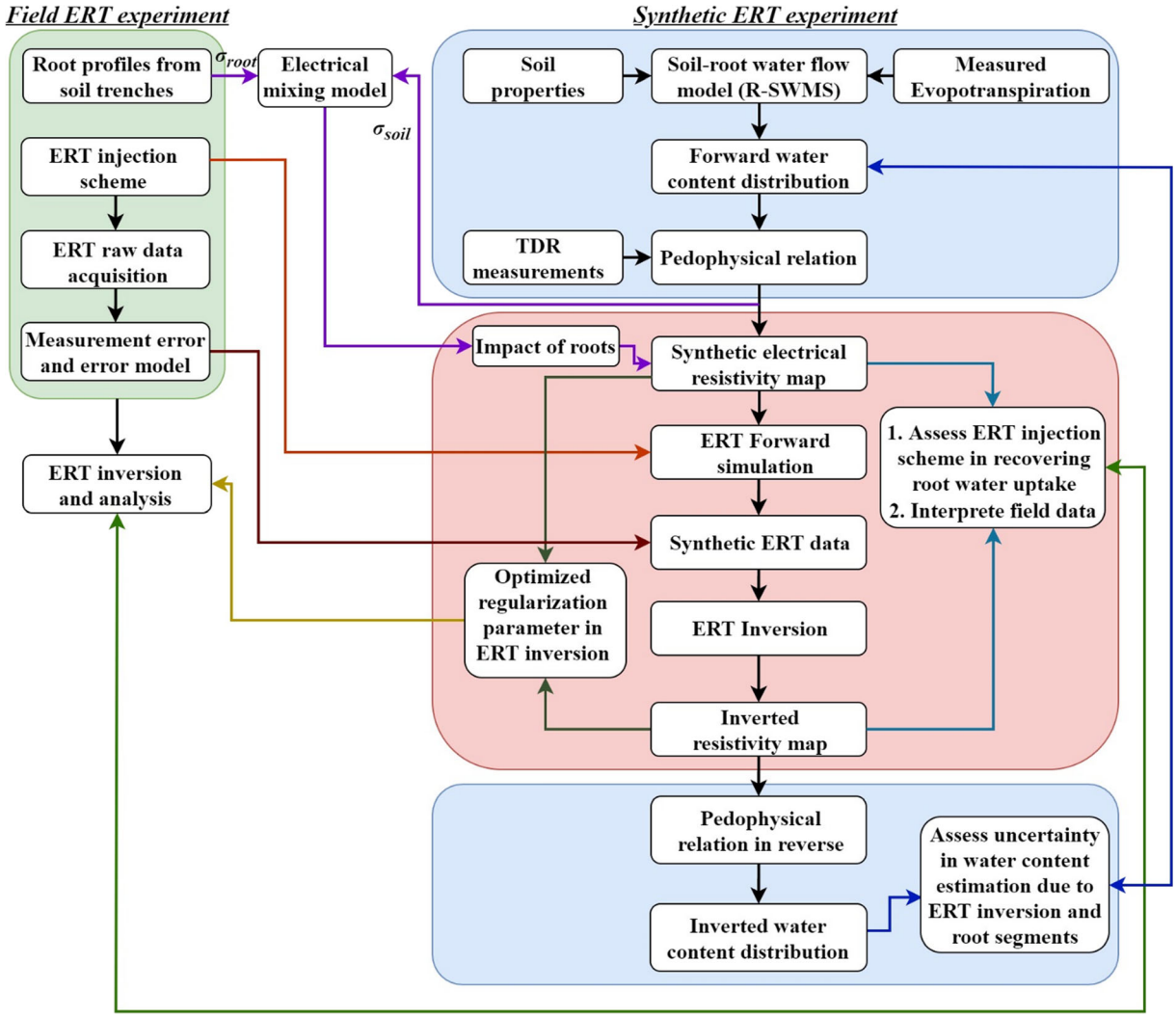

Fig. 4 Methodology for synthetic experiment and its relation to the field experiment, the blue area corresponds to water-flow simulations and the red area shows the ERT simulations. The region outside the red and blue areas corresponds to real field experiments

With this assumption, differences between root water uptake patterns will only be due to the difference between *RND* distributions and available water in the soil. This means that no differences between the root hydraulic properties of the different species were considered. The ET0 estimated from the weather station data was used as a plant flux boundary condition.

ERT simulations - generation of synthetic resistivity distributions

Modeled water content maps were transformed to electrical resistivity fields using Eq. 4. The pyGIMLi software was used for ERT forward simulations on the synthetic resistivity model, which solves Poisson's equation in 2.5-D to compute the modeled ERT data with the same injection scheme than in reality. The forward modeled ERT measurements were contaminated with Gaussian noise with an amplitude defined by the error model quantified for field data. Inversion of the modeled ERT data was performed using the same methodology as in the field. Different meshes were used for forward and inverse calculation to avoid inverse crime.

Gaussian fits

In WD treatment, any increase in electrical resistivity is supposed to be due to a water content decreased

generated by plant water uptake. The 2-D distributions of water content at t3 and t1 denoted by $\theta\,(t3)$ and $\theta\,(t1)$ are obtained by applying petrophysical relation (Eq. 4) to 2-D distributions of electrical resistivity at t3 and t1 denoted by $\rho(t3)$ and $\rho(t1)$. To characterize plant-specific depletion patterns, we compute the 2-D time difference of resistivity and water content defined as:

$$\delta\rho = \log(\rho(t3)) - \log(\rho(t1))$$

and the change of water content between t1 and t3 is defined as

$$\delta\theta = \theta\,(t3) - \theta\,(t1)$$

The 1-D medians at each depth from 2-D distributions of $\delta\rho$ and $\delta\theta$ was computed for each plant and a Gaussian curve was fitted to the 1-D medians of $\delta\rho$ and $\delta\theta$ profiles ($\delta\rho_{fit}$ and $\delta\theta_{fit}$):

$$\delta\rho_{fit} = a_{\delta\rho} * exp\left(\frac{-\left(\delta\rho - \mu_{Z,\delta\rho}\right)^2}{2*{\sigma_{Z,\delta\rho}}^2}\right) \quad (5)$$

$$\delta\theta_{fit} = a_{\delta\theta} * exp\left(\frac{-\left(\delta\theta - \mu_{Z,\delta\theta}\right)^2}{2*{\sigma_{Z,\delta\theta}}^2}\right) \quad (6)$$

From the fitted Gaussian function, the six parameters of a Gaussian function were then optimized to fit these 1-D profiles: $a_{\delta\rho}$, $a_{\delta\theta}$, $\mu_{Z,\,\delta\rho}$, $\mu_{Z,\,\delta\theta}$, $\sigma_{Z,\,\delta\rho}$ and $\sigma_{Z,\,\delta\theta}$. The mean parameter $\mu_{Z,\,\delta\rho}$ or $\mu_{Z,\,\delta\theta}$ represents the depth at which depletion is the largest (maximum depletion depth) while $\sigma_{Z,\,\delta\rho}$ or $\sigma_{Z,\,\delta\theta}$ represents the spread of the depletion as illustrated in Fig. 5a. The product of the amplitude parameter ($\sqrt{2\pi}a_{\delta\theta}$) with the spread ($\sigma_{Z,\,\delta\theta}$) represents the amount of abstracted soil water, which will be denoted by $A_{\delta\theta}$ [m].

Uncertainty in the petrophysical relation due to the presence of roots

To account for the uncertainty brought by the presence of roots on the petrophysical relation (Rao et al. 2019), we ran additional synthetic scenarios including the impact of root-specific electrical conductivity on the bulk conductivity map (Fig. 6). First, we transformed R-SWMS-simulated water content maps (θ_{R-SWMS}) into forward electrical resistivity map ρ_{soil} using the soil-specific petrophysical relation of Eq. 4. Second, the impact of root segments is added to the forward electrical resistivity map using the mixing model approach of Winchen et al. (2009). We do not consider root explicit architecture as in Rao et al. (2019) due to computational constraints at the field scale. Instead, a two-phase mixing model (Winchen et al. 2009) is used to compute the effective electrical conductivity bulk resistivity ρ_{mm} based on root resistivity (ρ_{root}) and soil resistivity maps (ρ_{soil}(X,Z)):

$$\rho_{mm} = \left[f\left({\rho_{root}}^{\alpha}\right) + (1-f)\left({\rho_{soil}}^{\alpha}(X,Z)\right)\right]^{\frac{1}{\alpha}} \quad (7)$$

where f is the relative area of root segments to the total area and $(1-f)$ is the relative area of the soil region. α is an exponent describing the geometry of two phases (soil and root): if soil and root component would be connected in series, then α would equal -1 and for perfectly parallel connection, $\alpha = 1$. In reality, the soil-root system represents a mixture of series and parallel connections, and hence, α captures this complex connectivity information. In this study, we assume $\alpha = 0.5$ which we obtained from a specific numerical experiment (see supplement S6).

The root fraction map was estimated based on the root number density map. We computed the root surface density by assuming a constant root diameter of 0.03 cm (Gibson 2009) and an averaged root length of 1,83 cm/cm^2 (Faye et al. 2019). Two scenarios were considered for ρ_{root} based on root measurements made by Ehosioke et al. (Ehosioke et al. 2018): 10 Ωm and 100 Ωm. Three scenarios were defined:

a) Scenario 1: ρ_{soil} derived from θ_{R-SWMS} is not contaminated with ρ_{root} in synthetic ERT experiment.
b) Scenario 2: ρ_{soil} derived from θ_{R-SWMS} is contaminated with $\rho_{root} = 10\Omega m$ in synthetic ERT experiment.
c) Scenario 3: ρ_{soil} derived from θ_{R-SWMS} is contaminated with $\rho_{root} = 100\Omega m$ in synthetic ERT experiment.

Results

ERT field experiment results: Qualitative comparison between WD and control conditions

In Fig. 6a and b, we show the inversion results of field data under control and WD conditions, respectively.

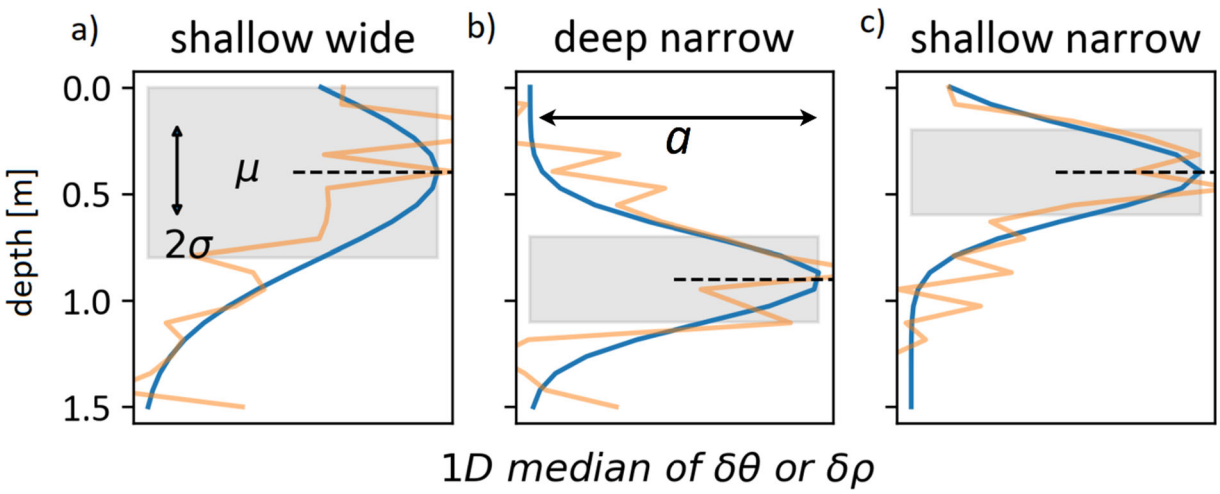

Fig. 5 Illustration of Gaussian fits for discriminating plant uptake behavior: **a**) plant uptake region is shallow but the spread is wide, **b**) uptake region is deeper while the spread is narrow, and **c**) uptake is shallow and spread is narrow. The yellow line indicates possible ERT observation while the blue line is the Gaussian fit. The gray shade indicates the uptake spread ($\sigma_{Z,\,\delta\rho}$ or $\sigma_{Z,\,\delta\theta}$) while dotted line indicates maximum depletion depth ($\mu_{Z,\,\delta\rho}$ or $\mu_{Z,\,\delta\theta}$) and the amplitude of the Gaussian peak is the depletion amount *a*

The inversion converged after 3 to 5 iterations with rrms <2 and $\chi^2 < 8$ (see the textbox to the right of Fig. 6a). Since we had higher measurement errors in the WD treatment, the inversion has higher χ^2 values as compared to the control treatment. Since only small regions show the log of resistivity higher than 2.2 or lower than 1.2 in both WD and control treatments, we cut our color scale from 1.2 to 2.2 in Fig. 6a and b to compare both treatments simultaneously.

Conspicuously, the impact of treatments WD versus control is well captured by the ERT imaging. WD plots are increasingly resistive from t1 to t3 whereas the opposite scenario happens for the control treatment. In the controlled plots, rainfall and soil infiltration decrease the electrical resistivity of the surface layer as shown by the fading red region in the top horizon ($Z < 0.3$ m) from t1 to t3. On the contrary, in the WD treatment, the root water uptake is the main driver of electrical resistivity changes. Indeed, such a process is highlighted by the widening drying front of the light green region (corresponding to $\log(\rho) = 1.75\ \Omega m$) from t1 to t3 in Fig. 6b indicating a deeper root water uptake ($Z <= -1$ m).

Some differences between plants are visible in Fig. 6 a and b for both control and WD conditions. In control, the region corresponding to $\log(\rho) = 1.56$ to $1.65\ \Omega m$ goes deeper ($Z > 0.5$ m) for plants R + WC and WC as compared to the plants C and R (Fig. 6a). Similarly, in WD, the region corresponding to $\log(\rho) = 1.75\ \Omega m$ goes deeper ($Z > 0.5$ m) for the first three plants (C, R + WC, and WC) compared to R (Fig. 6b).

The inversion results in both treatments show a slightly shallower depletion zone of R as compared to the first three plants (C, R + WC, and WC). However, large variability in electrical resistivity is also visible within plots, which makes the proper quantification of the depletion depth difficult to assess.

Synthetic experiments

Forward simulations

In Fig. 7a and b, R-SWMS simulations show contrasted soil water content patterns for control and WD treatments. In both control and WD treatments, we observe the effect of the root water uptake on the soil water content (dark brown patches in Fig. 7a and b). The water content distribution in the control treatment is quite homogeneous at depths below 0.75 m (Fig. 7a) while it is the opposite in the WD treatment (Fig. 7b). We see the impact of root water uptake in the WD treatment up to 1.5 m in depth (dark brown patches in Fig. 7b at $Z >$ 1 m). In control treatment (Fig. 7a), regular rainfall events between t1 and t3 (see Fig. 2b) fade out the soil water depletion pattern in the top 25 cm of the soil (increasing blue front in top 25 cm of Fig. 7a). In the WD treatment, we see the impact of root water uptake in the form of a deepening drying front between t1 and t3 (expansion of dark brown patches in Fig. 7b).

The differences between (C, R + WC, and WC) and R are evident in both treatments. The plant R does not

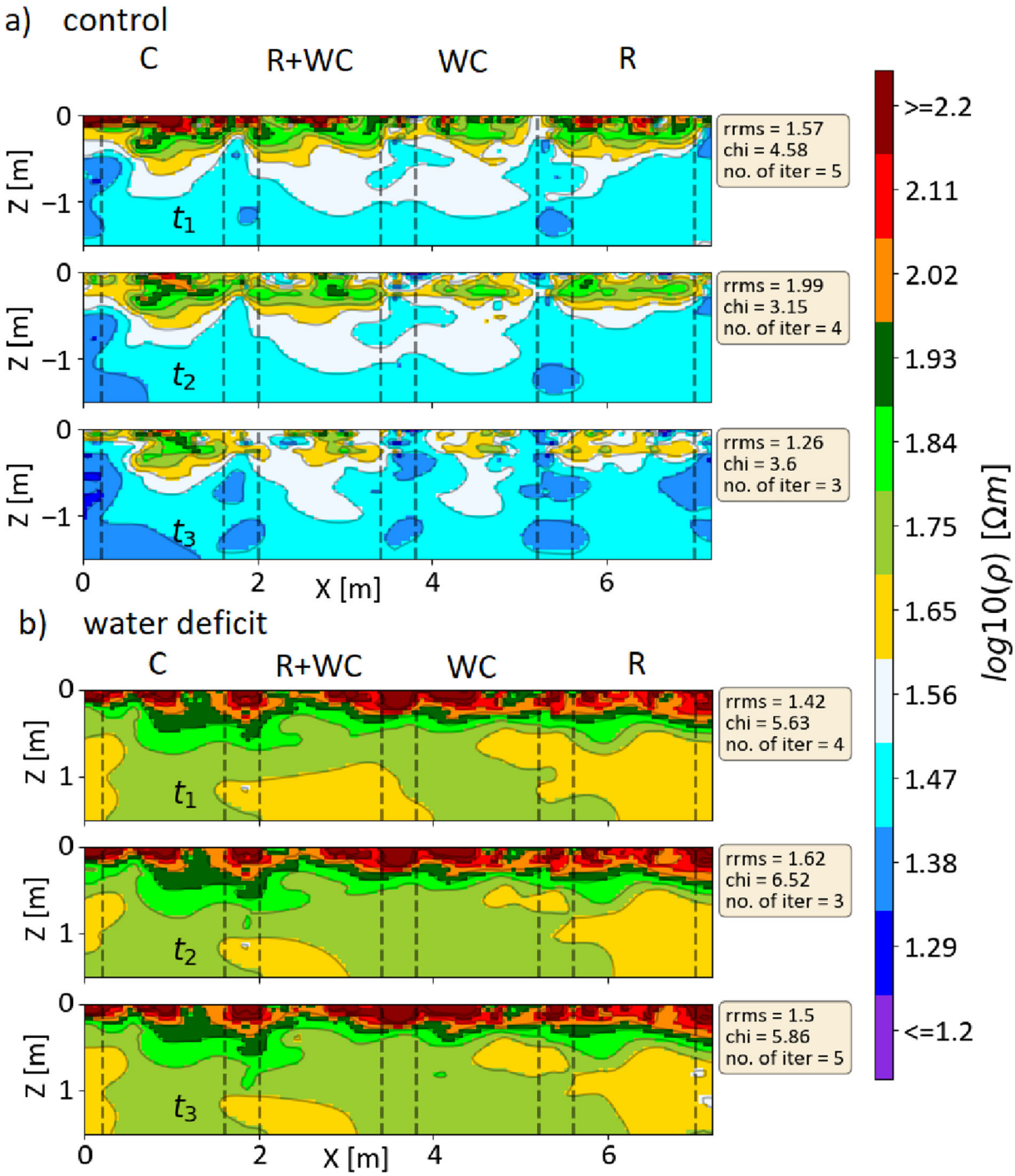

Fig. 6 Inversion results of field data at different times for **a**) control and **b**) water deficit treatments. Inversion quality parameters are shown to the right. The black dotted line represents the positions of different plants

go deeper than 30 cm while other plants influence the soil water content much below 30 cm (Fig. 7a). Although slight differences between species can be observed for the control treatment (Fig. 7b), the soil water content pattern evolution is mainly controlled by rain and not root characteristics.

Figure 7c and d show the corresponding electrical resistivity fields for the control and the WD treatments, respectively obtained with the petrophysical relations (Fig. 3). Similar to the field data in Fig. 6, only small regions in our synthetic experiment showed the log of resistivity higher than 2.2 or lower than 1.2 in both treatments. Therefore, we cut our color scale from 1.2 to 2.2 in Fig. 7c and d to compare both treatments simultaneously. Although the objective of the synthetic experiment was not to fit the field observations, we can still make a qualitative comparison of the observed patterns. The fading of the high resistive region ($\log(\rho) >= 2.2$) in the top horizon of the control condition in Fig. 7c closely resembles the experimental results of Fig. 6a. However, in the WD condition, comparing Figs. 7d and 6b show that field data are more resistive especially at depth $0.5\ m < Z < 1\ m$ and structurally more heterogeneous in terms of uptake front. These differences in resistivity magnitude in simulations and experiments can arise due to uncertainty in the petrophysical function used to convert R-SWMS water content to electrical resistivity.

ERT inversion

Figure 8 (a, c, e, g) shows the forward and inverted electrical resistivity (expressed as $\log\rho$) at t3 for the control treatment and the three scenarios under WD. We focused only on the first-meter depth, where the sensitivity is higher (see supplement material section C). In general, it is observed that the inverted $\log(\rho)$ field generally keeps the main features of the forward simulations. In general, the high-resistivity zones are retrieved for both treatments and all (combinations of) plant species. However, while the difference between species is visible in the control treatment, no obvious difference between patterns seems to appear in the WD treatment. Figures 8(e and f) show the forward and inverse resistivity maps for Scenario 2 and 3 in WD condition, where the impact of root resistivity was incorporated using a mixing model. Comparing Figs. 8b, e, and f, we see that the presence of roots increases electrical resistivity in some regions: for the yellow region ($\log(\rho) = 1.65$) in Fig. 8b to light green ($\log(\rho) = 1.75$) in Fig. 8e for Scenario 2 ($\rho_{root} = 10\ \Omega m$) and to dark green ($\log(\rho) = 1.84$) for Scenario 3 ($\rho_{root} = 100\ \Omega m$).

Figures 8(b, d, f, h) show the time difference or the change of log resistivity between t1 and t3 ($\delta\rho$) of the forward and inverted datasets for control and the three scenarios of WD. Areas with a positive $\delta\rho$ correspond to zones from which soil water is extracted. Forward simulations for the control treatment show no increase in electrical resistivity (Fig. 8b), probably due to the rainfall events. Even if, in general, the inversion recovered well the main patterns, no information on root water uptake depths can be inferred from the control treatment.

In the WD treatment, differences between species are much clearer in $\delta\rho$ (Fig. 8d) than in $\log(\rho)$ (Fig. 8c). Moreover, not only the magnitude of $\delta\rho$ but also its spatial distribution are affected by plant species. Although the sharp boundary of depleted zones is blurred in the inversion results in Fig. 8d, possibly due to the smoothness constraint in the ERT inversion, the ranking of plants uptake depth seems to remain. For example, notice the differences between (C, R + WC, and WC) and R in Fig. 8d. Comparing $\delta\rho$ of the three scenarios (Fig. 8 d, f, h) under WD show no significant differences illustrating the importance of using time-lapse to reduce uncertainty due to the presence of roots.

Using ERT to recover plant-specific depletion zones

Synthetic experiments

To better visualize differences between plant behaviors under WD conditions, plant-specific median profiles of several variables related to water depletion and Gaussian fit parameters are shown in Fig. 9 for scenario 1 (no additional impact of root segments in electrical resistivity forward map). The water depletion $\delta\theta$ profiles of the forward simulations (dashed black lines) is compared to inverted $\delta\rho$ profiles (dashed red profile) and to water depletion profile $\delta\theta$ obtained from inverted ERT (dashed blue line). Besides, the fits of a Gaussian distribution function on ERT-inverted $\delta\theta$ and $\delta\rho$ profiles are shown in the same colors (solid lines).

The use of a Gaussian function seems to be adequate to fit the depletion profiles in $\delta\theta$ or $\delta\rho$, as observed in Fig. 9a, which supports its use for further statistics. The comparison between forwarding $\delta\theta$ and inverse $\delta\rho$ profiles (black and red dashed lines) show some discrepancies. However, when pedophysical relations are used to retrieve $\delta\theta$ profiles (blue lines), the match to forward $\delta\theta$ (dashed black lines) improve significantly especially for WC and R. We observe that in general, inversely

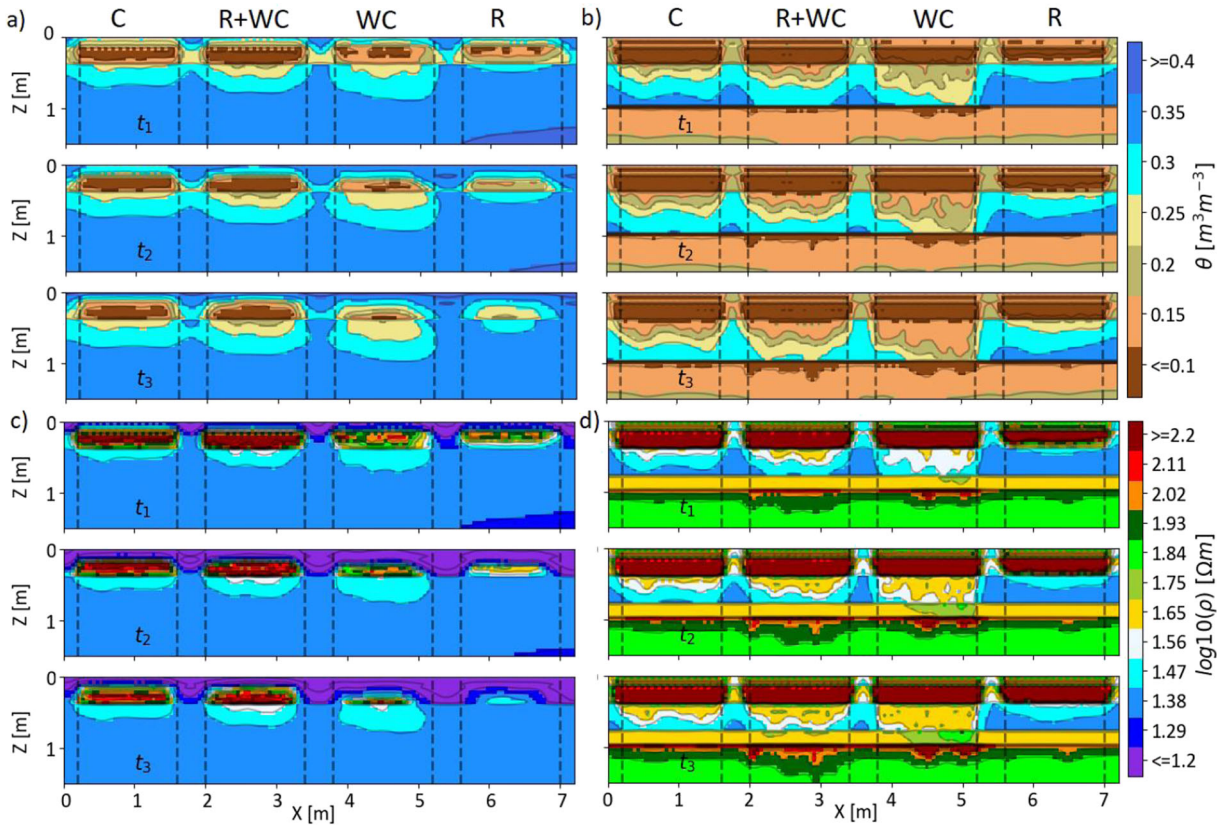

Fig. 7 Simulated evolution of water content (θ) distribution from t1 to t3: **a**) control treatment and **b**) water deficit treatment and its corresponding evolution of electrical resistivity (ρ): **c**) control treatment and **d**) water deficit treatment. The black dotted line represents the positions of different plants

retrieved $\delta\theta$ are more dispersed than direct $\delta\theta$ profiles, with lower peaks.

We used the Gaussian function parameters ($A_{\delta\theta}$, $\mu_{Z,\,\delta\rho}$, $\mu_{Z,\,\delta\theta}$, $\sigma_{Z,\,\delta\rho}$ and $\sigma_{Z,\,\delta\theta}$) and to compare the 1-D profiles in terms of water uptake, maximum depletion depth, and depletion zone spread, respectively. These statistics are shown in Fig. 9b and c for each (combination of) species and compared to the forward $\delta\theta$ statistics. Our forward simulations show a maximum depletion depth generally below 0.25 m with the following ranking: R < C < R + WC < WC. If we compare the $\mu_{Z,\,\delta\theta}$ to the $\mu_{Z,\,\delta\rho}$ obtained by inversion, we observe that the ranking between species is retrieved for all species. In general, the difference between forward and inverted maximum depletion depth is always lower than 10 cm. In terms of depletion spread, it is observed that ERT-retrieved $\sigma_{Z,\,\delta\rho}$ always overestimate forward $\sigma_{Z,\,\delta\theta}$. On the opposite, the match between forward and inverse $\sigma_{Z,\,\delta\theta}$ is remarkably good (less than 5 cm difference). The amount of depletion ($A_{\delta\theta}$) is retrieved well for C, WC and R but for R + WC we see that $A_{\delta\theta}$ is underestimated in Fig. 9f. The nonlinearity of the petrophysical relation explains why sometimes the use of $\delta\rho$ leads to the wrong estimate of $\mu_{Z,\,\delta\theta}$ or $\sigma_{Z,\,\delta\theta}$ or $A_{\delta\theta}$.

Uncertainty in Gaussian parameters

How the presence of electrically resistive roots affects the $\delta\theta$ profiles when we use a petrophysical relation that is valid for soil only is shown in Fig. 10a. As expected the more resistive the roots the larger the impact on the computed $\delta\theta$ (compare yellow curves to green curves in Fig. 10a). Interestingly, due to the nonlinearity of the petrophysical relation and the difference in the soil and roots resistivity maps, the impact of roots differs between species. Ryegrass (R) $\delta\theta$ profile is less affected by the presence of roots than the other (combination of) species. On the opposite, the impact of the presence roots on Cocksfoot (C) $\delta\theta$ profile is much bigger (with an error of around 4% of volumetric water content at the

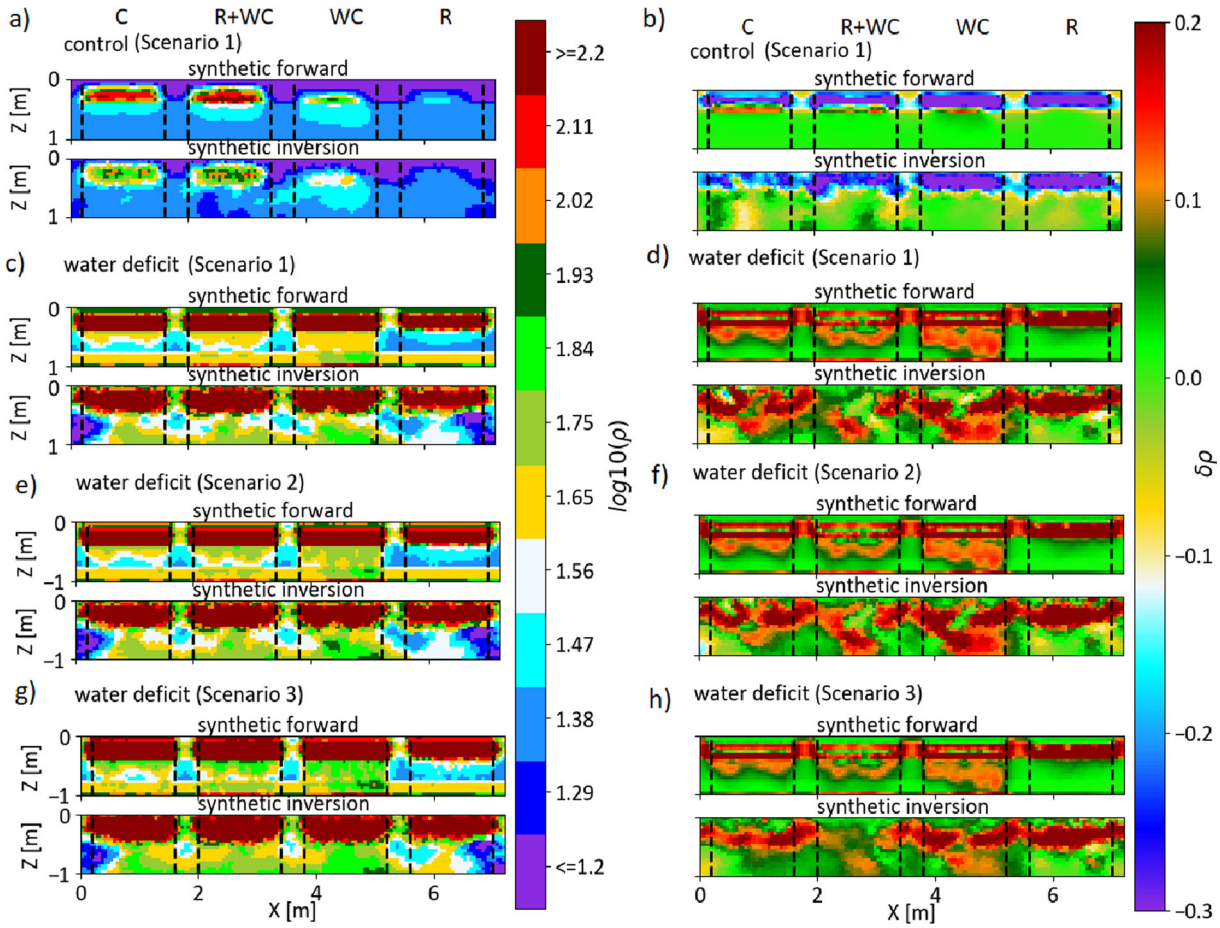

Fig. 8 Comparison of R-SWMS simulated forward data (first row) and ERT inversion of R-SWMS simulated data (second row). **a**) log(ρ) at t3 in control treatment for Scenario 1, **b**) The change of log resistivity between t1 and t3 ($\delta\rho$) in control treatment for Scenario 1, **c)** log(ρ) at t3 in water deficit treatment for Scenario 1, **d**) The change of log resistivity between t1 and t3 ($\delta\rho$) in water deficit treatment for Scenario 1, **e**) log(ρ) at t3 in water deficit treatment for Scenario 2, **f**) The change of log resistivity between t1 and t3 ($\delta\rho$) in water deficit treatment for Scenario 2, **g**) log(ρ) at t3 in water deficit treatment for Scenario 3, and **h**) The change of log resistivity between t1 and t3 ($\delta\rho$) in water deficit treatment for Scenario 3. The color bar in Figs. (a, c, e and g) has been cut at specified scale for visualization purposes. The black dotted line represents the positions of different plants

peak). In terms of $\delta\rho$ (not shown here) the maximum error induced by the presence of roots is 0.026 for scenario 2 and 0.08 for scenario 3.

The fitted Gaussian parameters (depletion depth, spread and amount) in water content namely $\mu_{Z,\,\delta\theta}$, $\sigma_{Z,\,\delta\theta}$ and $A_{\delta\theta}$ are shown in Fig. 10 for our three scenarios and compared to the forward R-SWMS parameters. In general, the presence of roots does not affect much the depletion depth (less than 5 cm between the 3 scenarios). The spread is a bit more affected (maximum error around 9 cm) and the depletion amount is the most sensitive parameter to the root presence, especially for scenario 3 (ρ_{root} = 100 Ωm). Despite these impacts, the ranking of species in terms of $\mu_{Z,\,\delta\theta}$ and $\sigma_{Z,\,\delta\theta}$ remains the same for the three scenarios, which indicates the robustness of our methodology. However, the impact of including roots on the amount of depletion $A_{\delta\theta}$ (Fig. 10c) is so large for scenario 3 that the ranking between species is not right anymore. Inclusion of root specific electrical property in the forward ERT tends to underestimate the water depletion in inversion, which is even enhanced with more resistive roots (scenario 3/ yellow bars).

In Table 2, we provide the relative percentage error in the Gaussian fit parameters between forward and ERT inversion for the three scenarios which varied between 0.02% to 43%. In scenario 1, the relative percentage error between forward and inverse indicates uncertainty arising due to ERT inversion only. The depletion spread

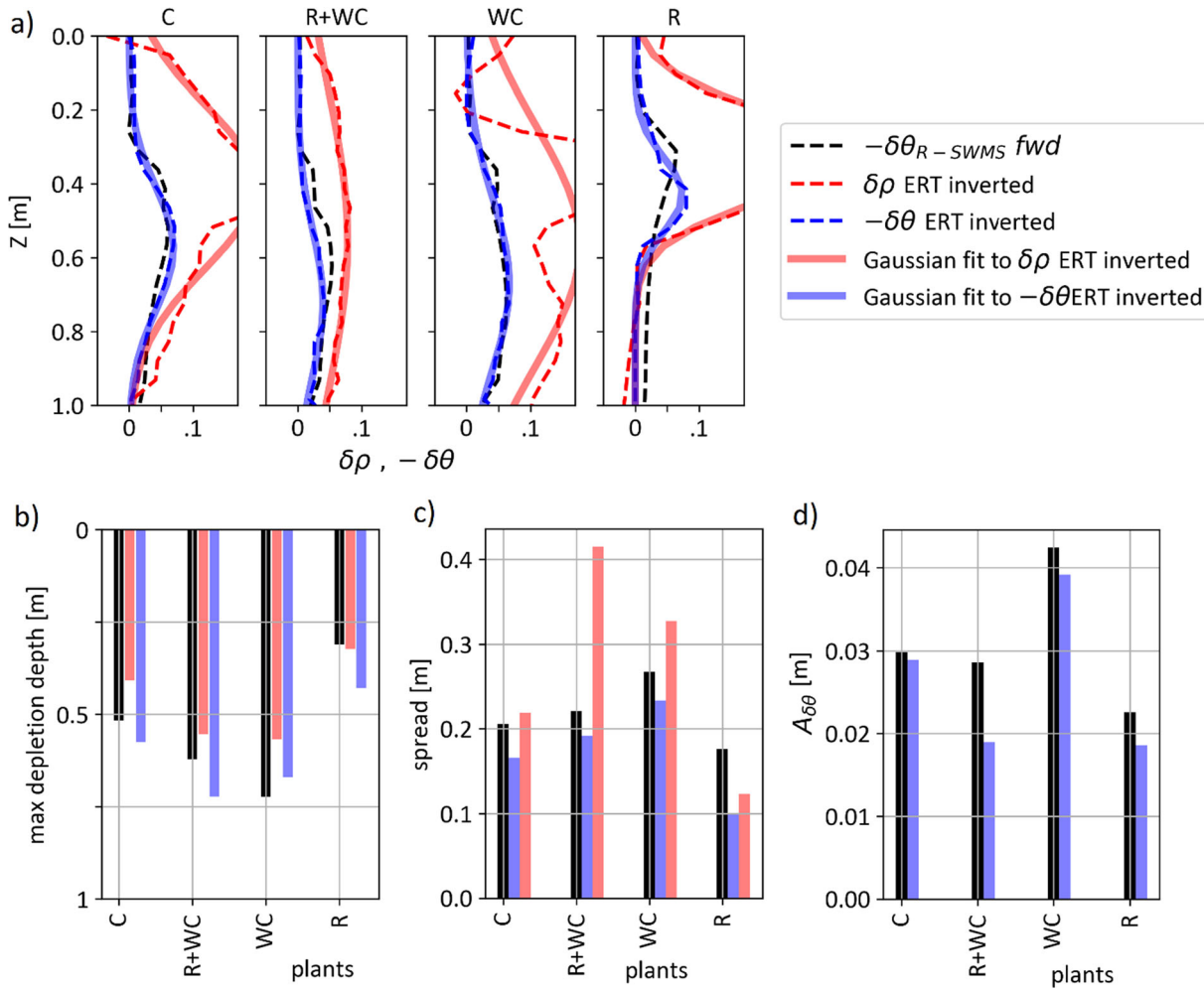

Fig. 9 **a**) 1D median of the change of log resistivity between t1 and t3 ($\delta\rho$) and negative of the change of water content between t1 and t3 ($\delta\theta$) for different plants in water deficit condition (dashed lines) and the Gaussian fit (solid line). The blue dotted lines represent -$\delta\theta$ derived from ERT inversion while the black dashed line represents the R-SWMS forward modeled -$\delta\theta$ (ground truth) **b**) maximum depletion depth of 1D median of $\delta\rho$ and -$\delta\theta$ as a function of plant species. The red solid lines represent $\mu_{Z,\ \delta\rho}$ derived from Gaussian fit to ERT derived $\delta\rho$, the blue solid lines represent $\mu_{Z,\ \delta\theta}$ derived from Gaussian fit to ERT derived -$\delta\theta$, while the black represents the maximum depletion depth of 1D median of R-SWMS forward modeled -$\delta\theta$. **c**) depletion spread of 1D median of $\delta\rho$ and -$\delta\theta$ as a function of plant species. The red solid lines represent $\sigma_{Z,\ \delta\rho}$ derived from Gaussian fit to ERT derived $\delta\rho$, the blue solid lines represent $\sigma_{Z,\ \delta\theta}$ derived from Gaussian fit to ERT derived -$\delta\theta$, while the black dashed line represents $\sigma_{Z,\ \delta\theta}$ derived from Gaussian fit to R-SWMS forward modeled -$\delta\theta$.d) depletion amount of 1D median of -$\delta\theta$ as a function of plant species [cm]. The blue solid lines represent $A_{\delta\theta}$ derived from Gaussian fit to ERT derived -$\delta\theta$, while the black line represents $A_{\delta\theta}$ derived from Gaussian fit to R-SWMS forward modeled -$\delta\theta$

($\sigma_{Z,\ \delta\theta}$) showed the highest uncertainty followed by depletion amount ($A_{\delta\theta}$) and depletion depth ($\mu_{Z,\ \delta\theta}$). The ryegrass had the highest uncertainty of 17% in $A_{\delta\theta}$ and 43% in $\sigma_{Z,\ \delta\theta}$. In scenarios 2 and 3, the relative error between forward and inverse indicates not only the uncertainty due to ERT inversion but also due to the contamination of petrophysical relation by root segments. In general, the uncertainty is higher in scenarios 2 and 3 than scenario 1. Comparing the uncertainty in $A_{\delta\theta}$, it is evident that electrical conduction via root segments can lead to inaccurate water content estimation (up to 42%) when using bare soil petrophysical relation.

Field data

Figure 11a and b show the retrieved $\delta\rho$ distributions of the field data for the control and the WD conditions. In

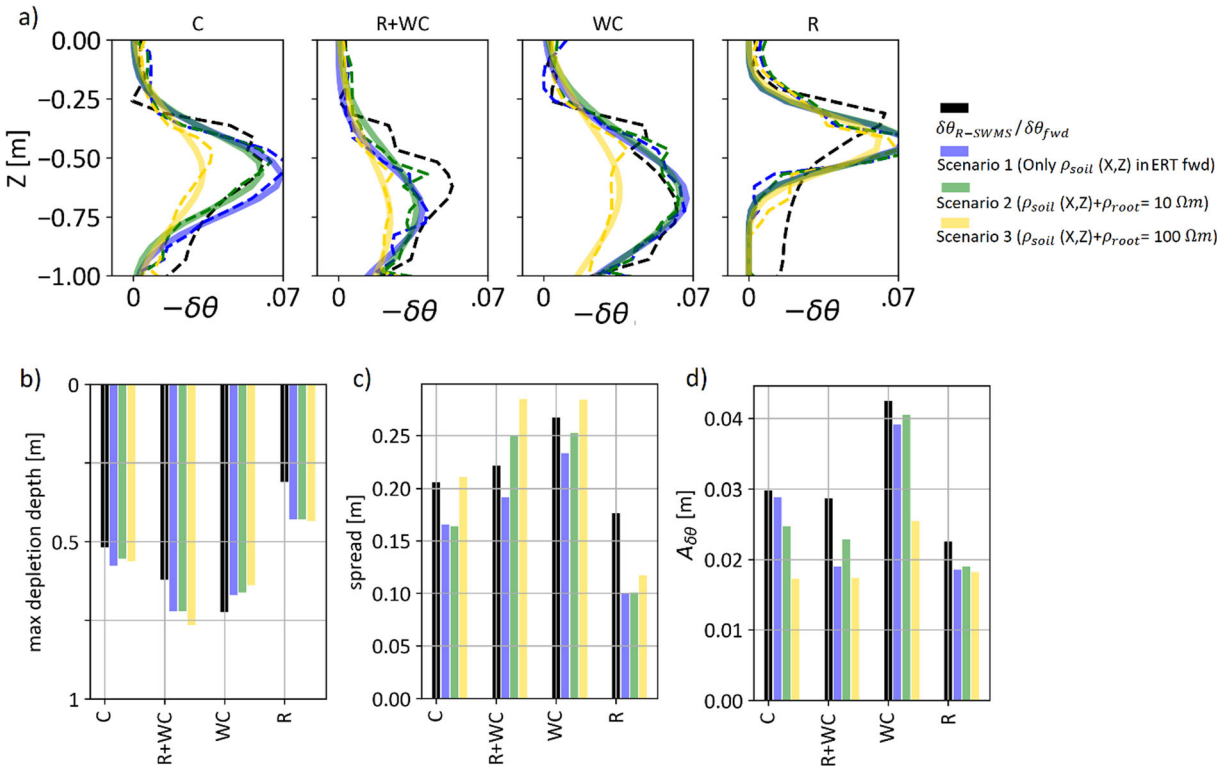

Fig. 10 Comparison between forward (R-SWMS) in black and ERT-derived 1D median of -$\delta\theta$ for the three scenarios (blue: Scenario 1, green: Scenario 2 and yellow: Scenario 3) as a function of plant species: **a**) 1-D median of negative change of water content between t1 and t3 ($\delta\theta$),**b**) depletion depth [m], **c**) depletion spread [m] and **d**) depletion amount [m]

agreement with the synthetic experiment, depletion zones are hardly visible in the control treatment. Root water uptake depletion zones are compensated by water infiltration and hide thereby plant-specific uptake patterns (Fig. 11a). We will, therefore, focus on the WD treatment data.

The comparison of Fig. 11b to Fig. 9d, reveals that resistivity change patterns in the field images are much patchier than those computed in the synthetic experiment. This can partly be associated with the inversion, which already generated patches in the synthetic experiment, as evidenced in Fig. 9d (bottom subplot). Also, variability in the actual soil hydraulic and petrophysical properties might have further increased the variability in $\delta\rho$ spatial field due to their nonlinearity.

Our synthetic experiments demonstrated that a 1-D profile of temporal changes helps visualize differences between species. We applied this method here to the $\delta\rho$ and $\delta\theta$ fields per plant (after using petrophysical relations). Figure 11c shows the $\delta\rho$ and $\delta\theta$ 1-D median profiles, together with the corresponding Gaussian fits. Large changes of resistivity are observed in the upper soil horizon (between 0 and 20 cm depth) of all plant plots. Yet, when we use the petrophysical relations to transform ρ to θ, these large $\delta\rho$ changes translate into much lower changes in terms of $\delta\theta$ (blue dashed lines in Fig. 11c). These large changes in resistivity observed in experiments (not observed in the model) are probably due to evaporation, which was not included in our synthetic experiment. To discriminate water uptake from evaporation impact on water depletion, we fitted the Gaussian relations on the $\delta\rho$ and $\delta\theta$ profiles only below 20 cm depth and above 0.8 m in depth due to poor sensitivity of ERT below 0.8 m depth (horizontal dashed lines in Fig. 11c).

Figure 11d and e show the parameters of the Gaussian fits: $\mu_{Z,\,\delta\rho}$, $\mu_{Z,\,\delta\theta}$, $\sigma_{Z,\,\delta\rho}$ and $\sigma_{Z,\,\delta\theta}$. The depths of maximum uptake zone μ_Z differ of maximum 5 cm between $\delta\rho$ and $\delta\theta$. Two groups of maximum uptake depths can be seen in Fig. 11d: shallower uptake for R and deeper uptake for C, WC, and R + WC. These maxima all occur below 0.5 m depth, where the root density (green curve in Fig. 11c) is relatively low. This is expected considering that in WD conditions, root

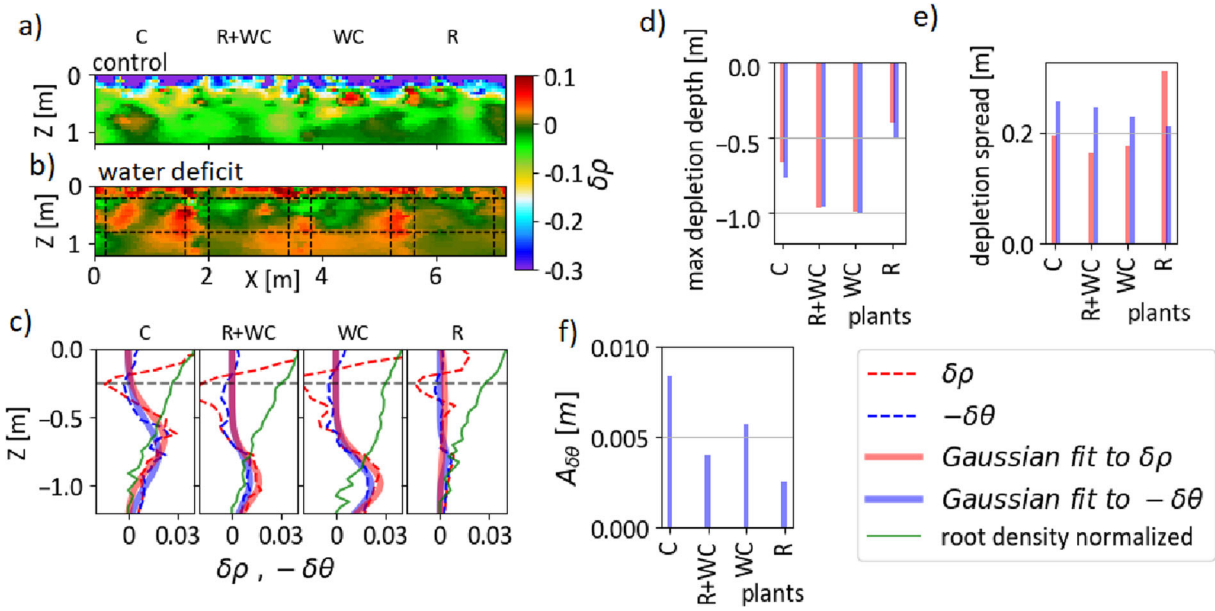

Fig. 11 Change of log resistivity between t1 and t3 of field inverted data ($\delta\rho$) for control and water deficit treatments. **a**) $\delta\rho$ in control treatment, **b**) $\delta\rho$ in water deficit treatment. The black dotted line represents limits between each plot/species. **c**) The 1-D median of $\delta\rho$ and $-\delta\theta$ for different plants in water deficit condition (dotted lines) and the Gaussian fit (solid line) and normalized root length densities (green line). The black dotted line represents the depth (Z = 0.25) above which data is discarded for Gaussian fit. **d**) maximum depletion depth of 1-D median of $\delta\rho$ and $-\delta\theta$ as a function of plant species. The red solid lines represent $\mu_{Z,\ \delta\rho}$ derived from Gaussian fit to ERT derived $\delta\rho$, the blue solid lines represent $\mu_{Z,\ \delta\theta}$ derived from Gaussian fit to ERT derived $-\delta\theta$. **e**) depletion spread of 1-D median of $\delta\rho$ and $-\delta\theta$ as a function of plant species. The red solid lines represent $\sigma_{Z,\ \delta\rho}$ derived from Gaussian fit to ERT derived $\delta\rho$, the blue solid lines represent $\sigma_{Z,\ \delta\theta}$ derived from Gaussian fit to ERT derived $-\delta\theta$. **f**) depletion amount of 1D median of $-\delta\theta$ as a function of plant species [m]. The blue solid lines represent $A_{\delta\theta}$ derived from Gaussian fit to ERT derived $-\delta\theta$

water uptake not only depends on root density but also on soil water availability, which is larger below the dry root zone. We can conclude from this trial that Cocksfoot (C), White clover (WC), and their combination (WC + R) have deeper depletion zones than ryegrass. However, the relatively flat measured $\delta\theta$ theta profile for R (Fig. 11c) casts some doubt on its representativity. The observed changes are probably in the range of uncertainty of the petrophysical model caused due to roots. Besides, in the synthetic study, the only difference between simulated species was their root distribution. In reality, there are a lot of other plant characteristics, which might affect their water uptake distribution, like plant root conductance, distribution of their hydraulic properties between root types, or their stomatal regulation.

In terms of uptake spread σ_Z, it is observed that R has a much higher spread than WC, WC + R, and C in $\delta\rho$ but not in $\delta\theta$. On the opposite of the synthetic experiment, we see that in general $\sigma_{Z,\ \delta\theta}$ is larger than $\sigma_{Z,\ \delta\rho}$ except for R. We conclude that Ryegrass has a much smoother and uniform uptake depth range than the other species. However, when we consider the amount of water depletion ($A_{\delta\theta}$), C is the highest water consumer followed by WC, R + WC and R consumed the lowest water (Fig. 11f).

Discussions

We conducted a high-resolution ERT study on an intercropped field trial with 3 different herbaceous species and one mixture subject to two different treatments (control and water deficit). The main aim of the study was to map the plant uptake response to drought (water deficit, WD) and investigate the sensitivity of ERT in capturing differences in water depletion patterns between species.

The synthetic analysis demonstrated that, despite higher smoothness due to inversion, the forward and inverse dry zones were relatively well retrieved in terms of the electrical resistivity (expressed in terms of the log ρ). However, differences between species were hardly visible. One-dimensional profiles of temporal

changes in median ρ or θ made the difference in depletion zones between species clearer. The ERT-retrieved $\delta\theta$ 1-D profiles were shown to match relatively well the actual depletion profiles. We fitted a Gaussian function to the 1-D profiles under WD conditions to retrieve five parameters: $A_{\delta\theta}$, $\mu_{Z,\,\delta\rho}$, $\mu_{Z,\,\delta\theta}$, $\sigma_{Z,\,\delta\rho}$ and $\sigma_{Z,\,\delta\theta}$. While the maximum depletion depths ($\mu_{Z,\,\delta\theta}$) were generally well retrieved in terms of $\delta\theta$ or $\delta\rho$ (maximum error of 10 cm) the spread of the depletion zone (σ_Z) was much better recovered using $\delta\theta$ (max error of 6 cm) than $\delta\rho$ (max error of 20 cm), demonstrating the importance of using petrophysical relations. These mean and standard deviations parameters in $\delta\theta$ were proved to adequately represent respectively the maximum depletion depth and the spread of the depletion zone. Uncertainty of the Gaussian parameters due to the presence of resistive roots was analyzed using synthetic experiments. We found that the presence of root segments might lead to the underestimation of about 40% of the amount of water depletion ($A_{\delta\theta}$). Yet, the ranking of species in terms of depletion depth and spread seemed to be unaffected by the presence of roots, showing the robustness of the approach for field phenotyping. This shows the importance of analyzing time-lapse water depletion information as against absolute electrical resistivity information. Therefore, we could use the fitted Gaussian parameters namely depletion amount, depletion depth and depletion spread as root phenotyping parameters in quantifying the water uptake ability of a plant in WD conditions. However, extending this approach to diverse crops, soils, and environments are needed to establish the methodology presented here. Also, the robustness of the method should be further investigated by including additional sources of uncertainty due to the regularization parameters in the ERT inversion, amongst others.

A very resistive and heterogeneous zone was observed in the upper soil horizon (between 0 and 20 cm depth) of all plots under WD condition. We attributed this effect on heterogeneous soil structure, surface evaporation, or increase in soil water salinity induced by evaporation. Future studies should focus on the variability of the petrophysical relation due to soil structure and changing pore water salinity.

When we use Gaussian fit indices for our real field data, we conclude that white clover (WC) (alone or in combination with Ryegrass) takes up water in deeper regions than the two other plants (Ryegrass and Cocksfoot). We also observe that Ryegrass has a more uniform water depletion (and hence uptake) profile, although the change in $\delta\theta$ is so small that it is within the uncertainty range of petrophysical relation due to roots (~ 0.01). In terms of the amount of water depletion, Cocksfoot consumes the largest amount of water despite having shallow roots followed by white clover, the combination of ryegrass and white clover, and ryegrass alone. This methodology should be tested on more plant species and at different scales.

The synthetic study also showed that differences between the plant uptake dynamics could better be characterized in WD conditions. Hence, plant phenotyping with ERT should ideally be realized under WD conditions. Yet, this study was performed for a relatively short (but realistic) WD period of three weeks. We expect that longer WD periods will enhance even more differences between species. Despite depth electrodes, we observe that the coverage is still low below 0.8 m depth. The installation of deeper electrodes and carefully optimized injection scheme is potentially needed to see deep root water uptake. Soon, we will use these Gaussian fit indices to assess their application on the whole field trial that includes additional species and their replicates.

Acknowledgments S. Rao was funded by the Fonds de la Recherche Scientifique – FRS- FNRS under Grant T.1088.15. The field trial was supported by the Région Wallonne under the project ForDrought D31-1341. We acknowledge Prof. Richard Lambert, Sébastien François, Maxime Doffagne, and Benjamin Van der Verren for providing the ERT data. We thank profs F; Nguyen, S. Garré, A Kemna, and N. Schwartz for their useful suggestions.

Data availability The field datasets acquired and analyzed in the current study are available at https://zenodo.org/record/3750199#.XpS-bVwzY2x, https://doi.org/10.5281/zenodo.3750199

Open Access This article is licensed under a Creative Commons Attribution 4.0 International License, which permits use, sharing, adaptation, distribution and reproduction in any medium or format, as long as you give appropriate credit to the original author(s) and the source, provide a link to the Creative Commons licence, and indicate if changes were made. The images or other third party material in this article are included in the article's Creative Commons licence, unless indicated otherwise in a credit line to the material. If material is not included in the article's Creative Commons licence and your intended use is not permitted by statutory regulation or exceeds the permitted use, you will need to obtain permission directly from the copyright holder. To view a copy of this licence, visit http://creative commons.org/licenses/by/4.0.

References

Ain-Lhout F, Boutaleb S, Diaz-Barradas MC, Jauregui J, Zunzunegui M (2016) Monitoring the evolution of soil moisture in root zone system of Argania spinosa using electrical resistivity imaging. Agric Water Manag 164:158–166

Amato M, Basso B, Celano G, Bitella G, Morelli G, Rossi R (2008) In situ detection of tree root distribution and biomass by multi-electrode resistivity imaging. Tree Physiol 28: 1441–1448

Atkinson JA, Pound MP, Bennett MJ, Wells DM (2019) Uncovering the hidden half of plants using new advances in root phenotyping. Curr Opin Biotechnol 55:1–8. https://doi.org/10.1016/j.copbio.2018.06.002

Beff L, Günther T, Vandoorne B, Couvreur V, Javaux M (2013) Three-dimensional monitoring of soil water content in a maize field using electrical resistivity tomography. Hydrol Earth Syst Sci 17:595–609. https://doi.org/10.5194/hess-17-595-2013

Benjamin M, Peruzzo L, Boaga J et al (2020) Time-lapse monitoring of root water uptake using electrical resistivity tomography and mise-à-la-masse: a vineyard infiltration experiment. Soil 6:95–114

Bergmann P, Schmidt-Hattenberger C, Labitzke T, Wagner FM, Just A, Flechsig C, Rippe D (2017) Fluid injection monitoring using electrical resistivity tomography—five years of CO2 injection at Ketzin, Germany. Geophys Prospect 65: 859–875

Besson A, Cousin I, Samouëlian A, Boizard H, Richard G (2004) Structural heterogeneity of the soil tilled layer as characterized by 2D electrical resistivity surveying. Soil Tillage Res 79:239–249

Bezerra-Coelho CR, Zhuang L, Barbosa MC, Soto MA, van Genuchten MT (2018) Further tests of the HYPROP evaporation method for estimating the unsaturated soil hydraulic properties. J Hydrol Hydromech 66:161–169

Boaga J, Rossi M, Cassiani G (2013) Monitoring soil-plant interactions in an apple orchard using 3D electrical resistivity tomography. Procedia Environ Sci 19:394–402

Brillante L, Mathieu O, Bois B, van Leeuwen C, Lévêque J (2015) The use of soil electrical resistivity to monitor plant and soil water relationships in vineyards. Soil 1:273–286

Cimpoiaşu MO, Kuras O, Pridmore T, Mooney SJ (2020) Potential of geoelectrical methods to monitor root zone processes and structure: a review. Geoderma 365:114232

Couvreur V, Vanderborght J, Javaux M (2012) A simple three-dimensional macroscopic root water uptake model based on the hydraulic architecture approach. Hydrol Earth Syst Sci 16(8):2957–2971

Dahlin T, Aronsson P, Thörnelöf M (2014) Soil resistivity monitoring of an irrigation experiment. Near Surface Geophys 12: 35–44

Dahlin T, Zhou B (2006) Multiple-gradient array measurements for multichannel 2D resistivity imaging. Near Surface Geophys 4:113–123

Ehosioke S, Sarah Garré, Kremer T, et al (2018) A New Method For Characterizing The Complex Electrical Properties of Root Segments. conference paper, 10th Symposium of the International Society of Root Research,July 2018, Israel. https://orbi.uliege.be/handle/2268/227107

Faye A, Sine B, Chopart J-L, Grondin A, Lucas M, Diedhiou AG, Gantet P, Cournac L, Min D, Audebert A, Kane A, Laplaze L (2019) Development of a model estimating root length density from root impacts on a soil profile in pearl millet (Pennisetum glaucum (L.) R. Br). Application to measure root system response to water stress in field conditions. PLoS One 14:e0214182

Garré S, Coteur I, Wongleecharoen C, Hussain K, Omsunrarn W, Kongkaew T, Hilger T, Diels J, Vanderborght J (2013) Can we use electrical resistivity tomography to measure root zone dynamics in fields with multiple crops? Procedia Environ Sci 19:403–410

Garré S, Javaux M, Vanderborght J, Pagès L, Vereecken H (2011) Three-dimensional electrical resistivity tomography to monitor root zone water dynamics. Vadose Zone J 10:412–424. https://doi.org/10.2136/vzj2010.0079

Gibson DJ (2009) Grasses and grassland ecology. Oxford University Press

Günther T, Rücker C (2006) A general approach for introducing information into inversion and examples from dc resistivity inversion. In: Near Surface 2006-12th EAGE European Meeting of Environmental and Engineering Geophysics. European Association of Geoscientists & Engineers, p cp-14-00060

Hansen PC (1992) Analysis of discrete ill-posed problems by means of the L-curve. SIAM Rev 34:561–580

Javaux M, Couvreur V, Vanderborght J, Vereecken H (2013) Root water uptake: from three-dimensional biophysical processes to macroscopic modeling approaches. Vadose Zone J 12(4): vzj2013.02.0042

Javaux M, Schröder T, Vanderborght J, Vereecken H (2008) Use of a three-dimensional detailed modeling approach for predicting root water uptake. Vadose Zone J 7:1079–1088. https://doi.org/10.2136/vzj2007.0115

Jayawickreme DH, Van Dam RL, Hyndman DW (2008) Subsurface imaging of vegetation, climate, and root-zone moisture interactions. Geophys Res Lett 35(18)

Koch A, Meunier F, Vanderborght J, Garré S, Pohlmeier A, Javaux M (2019) Functional–structural root-system model validation using a soil MRI experiment. J Exp Bot 70: 2797–2809

LaBrecque DJ, Miletto M, Daily W et al (1996) The effects of noise on Occam's inversion of resistivity tomography data. Geophysics 61:538–548

Leitner D, Meunier F, Bodner G, Javaux M, Schnepf A (2014) Impact of contrasted maize root traits at flowering on water stress tolerance - a simulation study. Field Crop Res 165: 125–137

Luo Z, Guan H, Zhang X (2019) The temperature effect and correction models for using electrical resistivity to estimate wood moisture variations. J Hydrol 578:124022

Manschadi AM, Christopher J, deVoil P, Hammer GL (2006) The role of root architectural traits in adaptation of wheat to water-limited environments. Funct Plant Biol 33:823–837

Mares R, Barnard HR, Mao D, Revil A, Singha K (2016) Examining diel patterns of soil and xylem moisture using electrical resistivity imaging. J Hydrol 536:327–338

Meister R, Rajani MS, Ruzicka D, Schachtman DP (2014) Challenges of modifying root traits in crops for agriculture. Trends Plant Sci 19:779–788. https://doi.org/10.1016/j.tplants.2014.08.005

Meunier F, Couvreur V, Draye X, Zarebanadkouki M, Vanderborght J, Javaux M (2017) Water movement through plant roots–exact solutions of the water flow equation in roots with linear or exponential piecewise hydraulic properties. Hydrol Earth Syst Sci 21:6519–6540

Meunier F, Heymans A, Draye X et al (2020) MARSHAL, a novel tool for virtual phenotyping of maize root system hydraulic architectures. In silico Plants 2:diz012

Michot D, Benderitter Y, Dorigny A, Nicoullaud B, King D, Tabbagh A (2003) Spatial and temporal monitoring of soil water content with an irrigated corn crop cover using surface electrical resistivity tomography. Water Resource Res 39:39. https://doi.org/10.1029/2002WR001581

Nichols SN, Hofmann RW, Williams WM, van Koten C (2016) Rooting depth and root depth distribution of Trifolium repens × T. uniflorum interspecific hybrids. Ann Bot 118:699–710. https://doi.org/10.1093/aob/mcw067

Paglis CM (2013) Application of electrical resistivity tomography for detecting root biomass in coffee trees. In: International Journal of Geophysics. https://www.hindawi.com/journals/ijge/2013/383261/. Accessed 26 May 2018, Application of Electrical Resistivity Tomography for Detecting Root Biomass in Coffee Trees

Panissod C, Michot D, Benderitter Y, Tabbagh A (2008) On the effectiveness of 2D electrical inversion results: an agricultural case study. Geophys Prospect 49:570–576

Passioura JB (2012) Phenotyping for drought tolerance in grain crops: when is it useful to breeders? Functional Plant Biol 39:851–859. https://doi.org/10.1071/FP12079

Pertassek T, Peters A, Durner W (2015) HYPROP-FIT software user's manual, V. 3.0. UMS GmbH, Munich, Germany

Rao S, Meunier F, Ehosioke S, Lesparre N, Kemna A, Nguyen F, Garré S, Javaux M (2019) Impact of maize roots on soil–root electrical conductivity: a simulation study. Vadose Zone J 18:190037

Rücker C, Günther T, Wagner FM (2017) pyGIMLi: an open-source library for modelling and inversion in geophysics. Comput Geosci 109:106–123

Srayeddin I, Doussan C (2009) Estimation of the spatial variability of root water uptake of maize and sorghum at the field scale by electrical resistivity tomography. Plant Soil 319:185–207

Tardieu F (1988) Analysis of the spatial variability of maize root density. Plant Soil 107:259–266

Vandoorne B, Beff L, Lutts S, Javaux M (2012) Root Water Uptake Dynamics ofCichorium intybusvar.sativumUnder Water-Limited Conditions. Vadose Zone J 11:11. https://doi.org/10.2136/vzj2012.0005

Whalley WR, Binley A, Watts CW, Shanahan P, Dodd IC, Ober ES, Ashton RW, Webster CP, White RP, Hawkesford MJ (2017) Methods to estimate changes in soil water for phenotyping root activity in the field. Plant Soil 415:407–422. https://doi.org/10.1007/s11104-016-3161-1

Winchen T, Kemna A, Vereecken H, Huisman J (2009) Characterization of bimodal facies distributions using effective anisotropic complex resistivity: a 2D numerical study based on Cole-Cole models. Geophysics 74:A19–A22. https://doi.org/10.1190/1.3113986

Publisher's note Springer Nature remains neutral with regard to jurisdictional claims in published maps and institutional affiliations.